COBEM 2023 27TH INTERNATIONAL CONGRESS OF MECHANICAL ENGENEERING

ABCM Brazilian Society of Mechanical Sciences and Engineering
27th ABCM International Congress of Mechanical Engineering
December 04-08, 2023, Florianópolis-SC, Brazil

COB-2023-1760
NUMERICAL SIMULATION OF THE ADDITIVE MANUFACTURING PROCESS BY LASER POWDER BED FUSION

Guilherme Sousa Moura
Diego Busson de Moraes
Gabriel Oliveira Rodrigues
Carolina Palma Naveira Cotta
Universidade Federal do Rio de Janeiro
guilherme.moura@poli.ufrj.br , busson@poli.ufrj.br , gabrielodst@gmail.com , carolina@mecanica.coppe.ufrj.br

Abstract. *The additive manufacturing (AM) process of Laser Powder Bed Fusion (L-PBF) is now as a popular technique for the fabrication of complex and intricate geometries in a wide range of materials. However, the control of the process parameters to achieve optimal quality of the printed part is still a challenge. In this work, we present a study that aims to understand the effects of the laser process parameters on the quality of parts produced using L-PBF. We focus on the alloy Remanium Star, which is widely used in dental and biomedical applications due to its excellent biocompatibility and mechanical properties. To this end, we carried out a series of single-track experiments varying the laser power and scanning speed and used the results to calibrate a numerical simulation model to further investigate the impact of the process parameters on the melt pool and part quality under different printing scenarios. This study contributes to the optimization of L-PBF process parameters for Remanium Star, and the insights gained can be applied to other materials and applications.*

Keywords: *Laser powder bed fusion, Numerical simulation, Process optimization, Additive manufacturing*

1. INTRODUCTION

Additive manufacturing has been gaining significant attention in recent years, especially in the most technological industries such as aerospace, biomedical, energy and automotive. The ability to produce small series of complex and customized parts with minimal lead times and reduced material waste has become increasingly important and is one of the pillars for the advent of Industry 4.0. Among the various additive manufacturing techniques, Laser Powder Bed Fusion (L-PBF) is one of the most promising technologies due to its high accuracy, potential for creating complex geometries and intricate internal features, versatility, amongst many other benefits. This process uses a high-energy laser to selectively melt and fuse thin layers of metal powder to, layer by layer, finally build a three-dimensional object.

As explained by Saunders (2017), the process occurs in a controlled environment with an atmosphere virtually depleted of oxygen or any other gases which might react with the molten metals and create undesirable incursions. To that end, the printing chamber is constantly supplied with a flow of inert gas, normally Nitrogen or Argon, which also serves in helping to remove heat from the melt pool as well as particles ejected from the powder bed during the process. On this last point, Bidare et al. (2018) present several close-up look videos of the melt pool which clearly show powder particles being drafted by the upward flow generated when the laser strikes the powder bed. Both these powder particles and a possible metallic gas cloud, if part of the melt pool surpasses the boiling point, can interfere with the laser beam and negatively affect the process. So, the constant flow of inert gas is very important to help in reducing this effect by carrying them away from the beam's path.

A depiction of the main elements of the L-PBF process is provided in Figure 1(a), which shows the standard arrangement contained within the inert environment, composed of three chambers. Initially, the powder supply chamber is filled with the desired metallic powder while the build plate in the print chamber is positioned on its maximum elevation. At the start of each cycle, the elevation mechanisms move in opposite directions, lowering the build plate by one layer thickness, usually 20-50 µm according to Loh et al. (2015), while exposing some powder from the supply chamber. The scrapper is then moved horizontally, spreading and slightly compacting the supplied powder into the print chamber and finally taking any excess powder to the outflow chamber. The laser is then turned on and follows a predefined path to melt the recently deposited powder in the desired areas, as well as part of the already solidified substrate beneath to ensure they fuse together. As the laser moves away, the molten region quickly cools down and the material solidifies. Passive or active lens systems are usually employed to guarantee a continuous focus adjustment of the laser as its unit is commonly static while its striking point moves around the print chamber, normally with the use of adjustable mirrors.

To print the slice of the final part present in each layer, the laser spot is normally moved along straight lines stacked laterally at a separation between scan vectors known as the hatch distance. Towards the end of the layer printing, the spot is moved at least once along the full outline of the section in order to reduce the stair stepping effect generated by the

stacking of the beads as shown in Figure 1(b). As depicted, the first line of movement along the contour is offset inwards by half of the expected bead width in order to ensure the correct sizing of the printed layer and a second offset or further offsets may be employed to guarantee a total consolidation of possible gaps between the hatch vectors and the outline bead.

The described cycle is repeated for each sequential layer, normally rotating the scan direction by a few degrees in order to reduce residual stresses, until the entire part is completed. In the end, the full print will be buried in and filled with unconsolidated powder which needs to be removed and combined with the powder in the outflow which can then be sieved and reused. Finally, the printed part, removed from the printer, can be heat treated if required and then mechanically removed from the build plate.

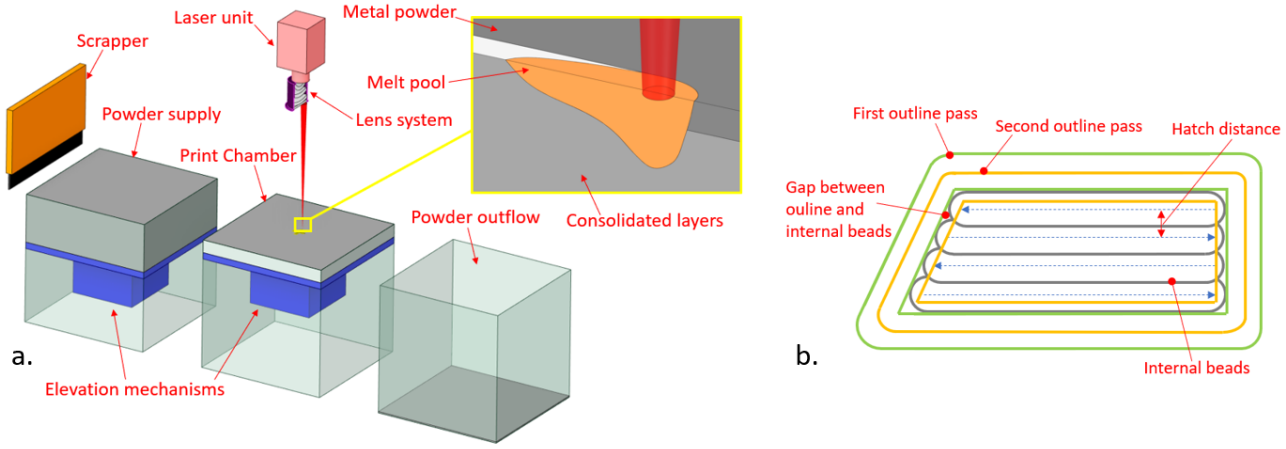

Figure 1. Schematic diagrams of the L-PBF Process: (a) Main Components; (b) Layer scan path

As pointed out in the study by Interreg Sudoe (2019), the process is highly dependent on the control of several parameters, such as the laser power and diameter, scan speed and layer thickness to name a few. These can significantly affect the microstructure, mechanical properties and level of consolidation of the final part. In fact, selection of proper parameters is always a balance between desired surface qualities, bulk properties such as yield strength or thermal conductivity and the process build rate. However, improper selection of process parameter combinations may create several types of defects both in the line, area or inter-layer formations. As cited by Yadroitsev (2009), these can come in the form of lack of proper fusion between adjacent layer or adjacent scan vectors, unstable lines presenting a balling or humping behavior, deep and unstable melt pools that may trap bubbles of the inert gas, amongst others. Therefore, a deep understanding of the L-PBF process and its parameters' influence on the part quality is crucial to optimize the process and develop reliable products for various applications.

Additionally, it is important to keep in mind that these process parameter combinations need to be tuned for each different material and/or powder granulometries, making the selection a time-consuming and expensive task by normally requiring an extensive experimental campaign. So, developing a methodology to more quickly define these parameters can greatly improve the efficiency, productivity and innovation rate of the L-PBF process. For that reason, many studies in recent years have focused in creating mathematical models to simulate with different degrees of fidelity the main phenomena of the process and thus allow for several insights to be drawn faster and cheaper than achieved solely with empirical methods.

Both Megahed et al. (2016) and King et al. (2015) present multiscale modelling approaches using a combination of very complete high fidelity, high accuracy costly models with simpler and coarser cheap models. The former include the geometries of the powder particles, fluid dynamics in the melt pool during melting and solidification, surface tension effects, laser absorptions and reflections on the particles and on the flow surface amongst other effects. These allow a very accurate representation of the melt pool and bead consolidation, but these models are extremely expensive to run, requiring normally days to weeks in order to simulate a single track formation and thus can only be used to generate very specific insights for a few parameter combinations. The same authors thus also present models in which the powder bed is represented as an effective medium, fluid dynamics are disregarded and laser-powder interactions are simplified in order to reduce computational costs and allow for bigger portions of the process or even full builds to be simulated and thus draw insights into interlayer defect formations or full volumetric phenomena such as residual stress deformations. These simpler models are normally calibrated against empirical results in order to guarantee their applicability.

Following this trend, the present study focused in developing a moderately cheap, empirically calibrated numerical model capable of providing insights about the impact of main process parameter combinations in the L-PBF printing of a relatively popular alloy, under the commercial name Remanium Star CL, but for which there are still very few studies. This alloy has a nominal composition of 60.5% Co, 28% Cr, 9% W and 1.5% Si plus other low concentration elements

and is best known for its high strength and biocompatibility being thus frequently used in the medical field, especially in dentistry applications.

2. EXPERIMENT

The focus of this study was primarily on the formation of printed traces, which are the fundamental elements in the construction of any L-PBF component. Therefore, the experiment was centered on the impact of the two main laser parameters, power and speed, on the quality of individual printed traces.

2.1 Procedure

The printer used was the Concept Laser Mlab Cusing 200R, manufactured by GE Additive. It contains a continuous-wave Yb:YAG fiber laser with a maximum power of 200W and a wavelength of 1070 nm. The laser focusing diameter was set to 50 µm and the machine has a maximum laser scanning speed of 7m/s. The powder used was composed of 10-30 µm mostly spherical particles of Remanium Star CL according to Dentarum (2022).

Following the procedure presented by Shahabad et al. (2020) to conduct a similar experimental campaign on a Hastelloy X alloy powder, a base was printed with an already available suitable parameter combination, which had been commercially acquired, and then traces with different combinations of speed and power were generated. Though requiring an already stablished proper combination, this strategy is interesting because it ensures that the study's traces are printed on a controlled substrate entirely formed by the printing material. Some other authors print the study traces on the first printing layer but then it is necessary to ensure that the machine's printing base has the same chemical composition as that of the powder or to account for the effect of different compositions between base and powder.

Utilizing almost the entire available space on the print bed and avoiding close proximities to its boundaries, a total of six base plates containing six different traces each were printed together in the configuration presented in Figure 2 (a). Additionally, it was decided to print three repetitions of each parameter combination to generate results in different regions of the print field and thus attempt to reduce the overall influence of effects such as laser inclination, local inert gas flow, and slight misalignments of the print bed. So, the three realizations of the 12 parameter combinations, named from C1 to C12 in Figure 2 (b) and with values listed in Table 2, were spread trying to create an even distribution within the print bed. Finally, a layer thickness of 30 µm was used to print the artefacts, an offset of 3mm to the base plate was added with fin supports for ease of removal and an identification number was printed on the lateral side of each plate for later identification as depicted on the final printed parts of Figure 2 (c).

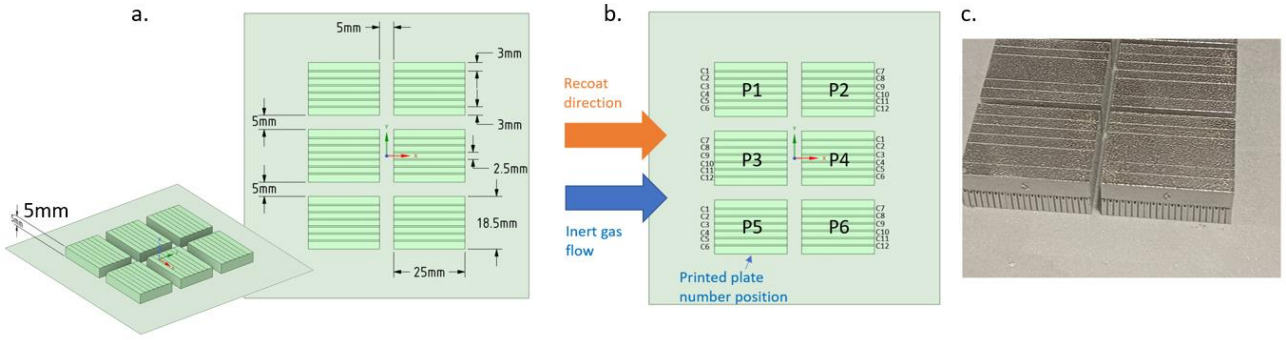

Figure 2. Experimental configuration: (a) print layout; (b) printed plate with 6 experimental traces

2.2 Experimental Results

The plates were removed from the base and each one of the printed tracks was analyzed along its entire length under a Hirox 3D KH8700 digital microscope in order to evaluate its quality and measure the characteristic width. As the quality and stability of each track has no fully objective definition, a quantitative score for different track regimes was defined and used to characterize the experimental results, examples of each regime and their associated scores are presented in Table 1. The lines appearing on the background of each experimental track are a view of the top layer of the printed plate, for which the scan direction was angled with respect to the final tracks.

The measurements and characterizations of each single track are summarized in Table 2 and a contour of a linear interpolation of the average scores over the design space is presented in Figure 3. The analysis of the score contour clearly shows a trend towards the formation of better traces with higher powers associated with lower speeds. Considering that the commercial parameter for internal filling is located in a zone where the score indicates the formation of unstable traces, it demonstrates that these zones are still applicable for general prints. Although this study only focuses on

individual traces, it is possible that the adjacent formation of new traces will fill in the small discontinuities or instabilities observed in the individual tracks.

Therefore, there is an apparent boundary of applicability along the line connecting the point (80W, 500 mm/s) to the point (200W, 2000 mm/s), with the entire region below it being applicable for internal filling formation. As for the contours, where there will be no possibility of straightening the traces through the remelting caused by adjacent traces, parameters that ensure greater stability of the trace are recommended. Thus, combinations within the red zone in Figure 3 should be chosen.

Table 1. Quantitative scores of printed tracks.

Condition	Lack of Fusion	Full Balling	Mild Balling	Unstable track	Continuous
Example	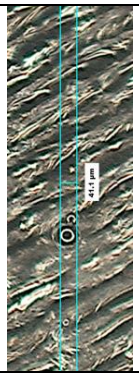	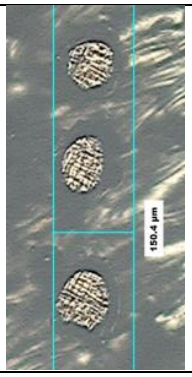	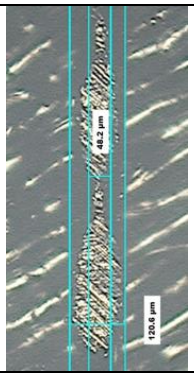		
Score	0	1	2	3	4

Table 2. Experimental measurements and scores.

Combination	**1**	**2**	**3**	**4**	**5**	**6**
P (W)	50	100	150	200	50	100
V (mm/s)	500	500	500	500	1250	1250
Thicknesses (µm)	130.5; 150.4; 68.1	120.6; 68.1; 62.4	127.7; 89.4; 75.2	161.7; 99.3; 79.4	0; 0; 0	167.4; 119.1; 83.7
Scores [Average]	1; 1; 1 [1.00]	2; 3; 3 [2.67]	2; 4; 4 [3.33]	2; 3; 4 [3.00]	0; 0; 0 [0.00]	1; 1; 1 [1.00]
Combination	**7**	**8**	**9**	**10**	**11**	**12**
P (W)	150	200	50	100	150	200
V (mm/s)	1250	1250	2000	2000	2000	2000
Thicknesses (µm)	59.8; 61; 62.4	59.6; 56.7; 59.6	0; 0; 0	0; 0; 0	68.1; 65.2; 63.8	65.2; 56.7; 56.7
Scores [Average]	3; 3; 3 [3.00]	3; 3; 3 [3.00]	0; 0; 0 [0.00]	0; 0; 0 [0.00]	1; 3; 1 [2.33]	3; 3; 3 [3.00]

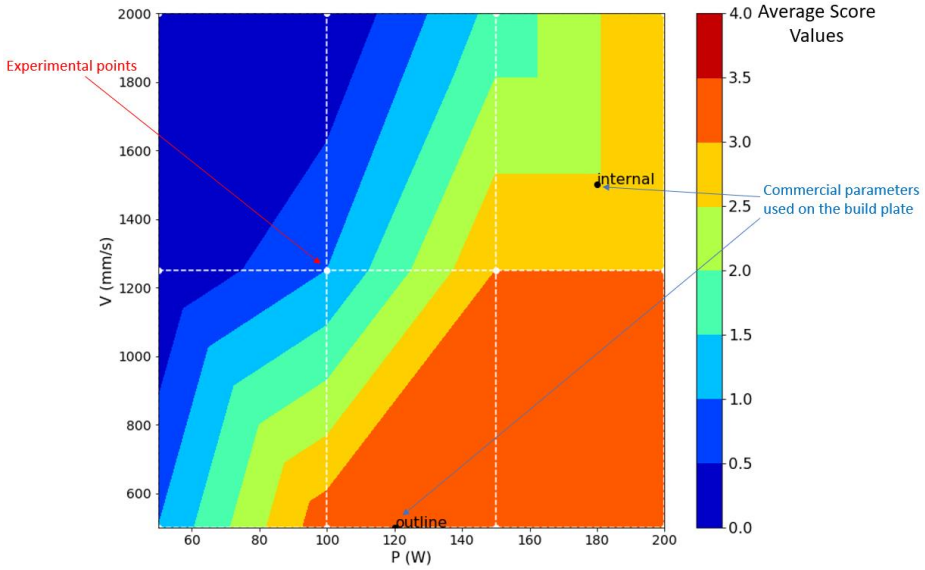

Figure 3. Contour of experimental scores

3. NUMERICAL MODEL

Expecting the need to run a large number of simulations, a more simplified modeling of the physical phenomena was chosen in order to reduce the cost of each calculation and ensure the evaluation of various combinations within a feasible time frame. Thus, a thermal diffusion modeling in a porous continuous medium was chosen to simulate the printing process of an individual trace. The dynamics of the melt pool weren't simulated, but an attempt was made to approximate its impact on the energy transport through an anisotropy factor. Additionally, its dimensions were estimated through the analysis of the calculated temperature fields where values exceeded the base material's melting temperature.

3.1 Material Properties

As there is virtually no experimental information about high temperature material properties of the Remanium Star alloy, values for similar CoCr alloys and a metallurgical simulation software, Thermo-Calc , were used to estimate the values required for the simulations. Moreover, the latent heat and temperature of evaporation for the alloy had to be estimated based on a compound average of the values for their main constituent elements, thus disregarding cross effects and arriving at values of 6.632 $\frac{\text{MJ}}{\text{kg}}$ and 3311K respectivelly.

To simulate the powder layer density and thermal capacity an effective medium approach was used in which the porosity (ϵ) of the medium was taken into consideration. This was considered to be of 50% based on the assertion of Gusarov et al. (2009) which places L-PBF powder beds in the 40-60% range due to the light compaction offered by the scrapper rollers. For the conductivity of the powder bed, a more sophisticated model had to be employed once, as stated by Batchelor and O'Brien (1977), heat transfer across the particles is quite complex, involving conduction through particle contacts but with energy mainly transferred through the permeating gas and radiation. For that end, the models presented by de De Moraes and Czebanski (2018) were used to estimate both the effective thermal conductivity in the powder medium and its emissivity (ϵ).

Finally, Figure 4 presents the thermal properties considered in the simulations. As can be observed, it is considered that the powder behaves in the same way as the base metal above the liquidus temperature (T_l), with its transition starting from the solidus temperature (T_s). Additionally, complete densification of the powder is assumed to occur once the liquidus temperature is exceeded, leading to the assumption that the porosity in this region becomes zero, and therefore the material at this point behaves with the properties of the bulk. Shrinkage of the recently melted region is disregarded as there is usually a draft of powder positioned adjacent to the melted region, which feeds the melt pool with additional material and effectively maintains approximately the initial equivalent volume.

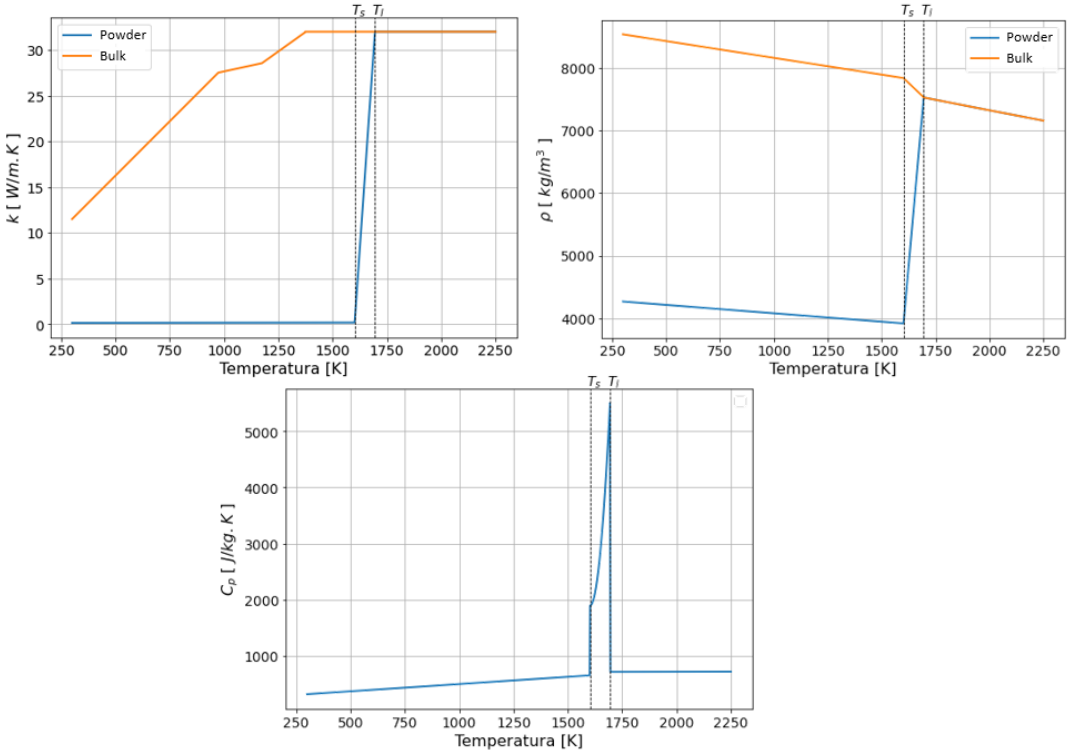

Figure 4. Powder and bulk material properties for the Remanium Star alloy:
k - thermal conductivity; ρ - density; c_p - specific heat

3.2 Mathematical model

The printing process was modeled through Eq.1 as a thermal diffusion process in a continuum with the laser absorption acting as a volumetric heat source (S_e) and modeled according to Eq.2 based on the studies of Zhang et al. (2019). As proposed by Safdar et al. (2013) the α and β factors are respectively an anisotropic and an isotropic conductivity factors in order to account for the increased heat exchange promoted by the melt pool dynamics and its preferential transversal transport direction driven mainly by the Marangoni Effect. These factors are both set to 1 beneath the material's liquidus temperature and set to calibrated constants above this temperature. Additionally, in following equations, ρ represents the density, c_p the specific heat, t time, k the thermal conductivity, T is temperature, η the laser absorption efficiency of the medium, P and r_l the laser's power and spot radius, d its penetration depth while x,y,z are the cartesian coordinates and x_l and z_l the local positions with respect to the center of the laser spot.

$$\rho\, c_p \frac{\partial T}{\partial t} = -\nabla \cdot \left(-\beta \begin{bmatrix} k & 0 & 0 \\ 0 & k & 0 \\ 0 & 0 & \alpha\, .k \end{bmatrix} \nabla T \right) + \mathrm{S_e}\ , \tag{1}$$

$$\mathrm{S_e}(x,y,z) = \eta \frac{2P}{\pi\, r_l^2}\, e^{-2\frac{\left(x_l^2+z_l^2\right)}{r_l^2}} .\frac{1}{d}\, e^{-\frac{|y|}{d}}\ , \tag{2}$$

As stated by Wang et al. (2002), the laser radiation penetrates the powder bed suffering several reflections and absorptions in the process which leads to much higher absorption rates than those normally observed for bulk metal surfaces. Exact values obviously depend on the material, particle shapes and their surface condition, granulometry, wavelength and more and are thus normally hard to pinpoint. For the present study, the total absorption factor η was estimated as being of 0.6 based on the experimental value found by Tolochko et al. (2000) for a similar CoCr alloy powder. As for the laser penetration depth (d), it was considered as being equal to the powder layer thickness once this value is orders of magnitude greater than the penetration experienced on the bulk material beneath.

To model the boundary conditions, considering a sufficiently large geometry so that the lateral and bottom boundaries have a negligible impact on the laser striking region, a constant room temperature of 300K was prescribed on these surfaces. For the top surface of the model, heat losses due to convection, radiation and evaporation were modelled according to Eq.3 in which ϵ is the powder emissivity and h was estimated at $15\frac{\mathrm{W}}{\mathrm{m^2K}}$ following the reference of Siao and

Wen (2022). L_v is the latent heat of vaporization and the mass flux $\dot{m}_v''$ was modelled according to Eq.4 as proposed by Siao and Wen (2022). Finally, as the vapor pressure (P_v) of the material was not available, it was modelled according to the Clausius-Clapeyron relation presented in Eq.5 which considers the evaporation temperature T_v, the molar mass M and the universal gas constant R_g.

$$q''_{top} = \text{h}\,(T - T_{amb}) + \epsilon\,\sigma\,(T^4 - T_{amb}^4) + \dot{m}_v''\,.\,L_v\,, \tag{3}$$

$$\dot{m}_v'' = P_v\sqrt{\frac{M}{2\pi R_g T}}\,, \tag{4}$$

$$P_v(\text{T}) = P_{atm}.\exp\left(\frac{L_v.M.(T-T_v)}{R_g.T.T_v}\right), \tag{5}$$

3.3 Solution and Post-Processing

The mathematical model was implemented and simulated in Ansys Fluent, a finite-volumes solver, using a first order implicit transient formulation with a second order upwind spatial discretization scheme. Considering the case of a single track printed on top of a consolidated base, a geometry as depicted in Figure 5 with two regions and considering symmetry along the XY plane was created. The length, height and width were defined to be sufficiently large to avoid boundary effects on the melt pool and both the maximum time-step size and the mesh were defined through refinement studies. The latter has a clearly higher discretization in the region slightly prior to the laser start position and extending a little further than its maximum travel distance in the simulations. The final mesh featured a total of 2000889 elements with the smallest ones along the top center line measuring 4.0µm x 1.6µm x 3.1µm along X, Y and Z directions.

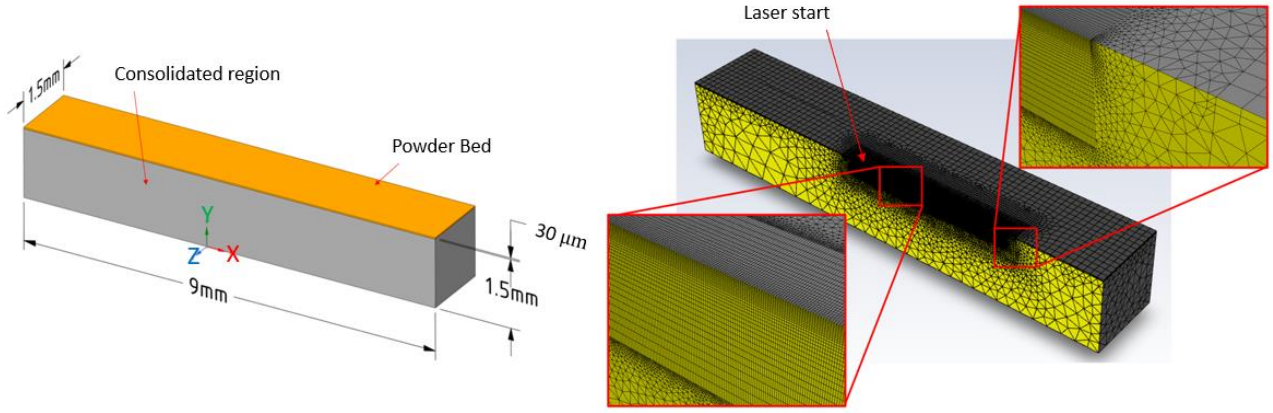

Figure 5. Geometry and Mesh for the single track simulations

The distinct powder and bulk material properties were assigned accordingly in the geometry and an adiabatic condition was applied to the central surfaces in order to enforce the symmetry. While running each simulation, the calculated nodal temperatures were saved at certain time points. These discretized results were then interpolated by inverse distance weighting, allowing for the melt pool surfaces to be estimated through a root finding algorithm along different lines by searching for the point at the material's solidus temperature. A fitting procedure was then used to find values for the α and β factors which minimize the total squared difference between numerical and experimental track widths.

With these defined, several different laser power and speed combinations were simulated. Then, to estimate the quality of the printed track in each of these, a procedure similar to that used by Johnson et al. (2019) of setting thresholds for the values and ratios between the melt pool (MP) dimensions was implemented. A minimum MP depth of 1.5 times the powder layer thickness was set as required to avoid the possibility of lack of fusion defects by improper interlayer consolidation. Configurations in which this criterion was not met were assigned a score of 0, in line with the grading used for the experimental campaign.

Finally, to estimate the linear stability of the track, the ratio between MP length and width was used. To take into consideration the different stability regimes from fully continuous all the way to full balling, the conservative threshold used by Johnson et al. (2019) of L/W < π was considered to be the onset of track instabilities while the more permissive threshold reported by Gunenthiram et al. (2017) through imaging experiments of L/W < 5 was used as the onset of full balling formation. So, configurations displaying a ratio of length and width smaller than pi were considered fully continuous and thus graded with 4, while ratios higher than 5 led to a grade of 1 for full balling, while intermediate ratios received grades interpolated between those two ends.

3.4 Numerical Results

The initial transient phase, where the dimensions of the melt pool vary before stabilizing, was examined to ensure consistent and stable simulation results. Four simulations with different laser power (50W and 200W) and laser speeds (0.5m/s and 2m/s) were performed, and the length, width, and depth of the melt pool were measured at various points during the simulations. As shown in Figure 6, all dimensions quickly stabilized with only minor fluctuations around a mean value. The width and depth stabilize within the first 250µm while the length takes a little bit longer but stabilizes within the first 500µm.

Moreover, the results revealed a direct relationship between laser power and the stabilization distance of the melt pool. Lower laser power led to quicker stabilization, with the melt pool reaching a stable state at approximately half the distance compared to higher power. This finding is particularly relevant for printing small-sized features, as it suggests that lower power settings may improve consistency and quality by allowing for complete melt pool stabilization. Additionally, the analysis indicated that laser speed had minimal impact on the stabilization distance of the melt pool.

Lastly, a jump before stabilization can be observed for the length in the simulation with 50W and 2m/s. This anomaly is due to the shallow depth of the melt pool obtained with these laser parameters. The calculated MP depths for this simulation are practically the same as the powder layer thickness, 30µm. Therefore, in the initial stage of the simulation, the melt pool encounters significant resistance to conduct heat to the underlying substrate, and the preferred path becomes the already solidified tail of the trace, causing it to grow rapidly. However, once the depth of the melt pool reaches at least the thickness of the powder layer, the substrate becomes the preferred path for heat dissipation from the melt pool, leading to a rapid decrease in the melt pool's length.

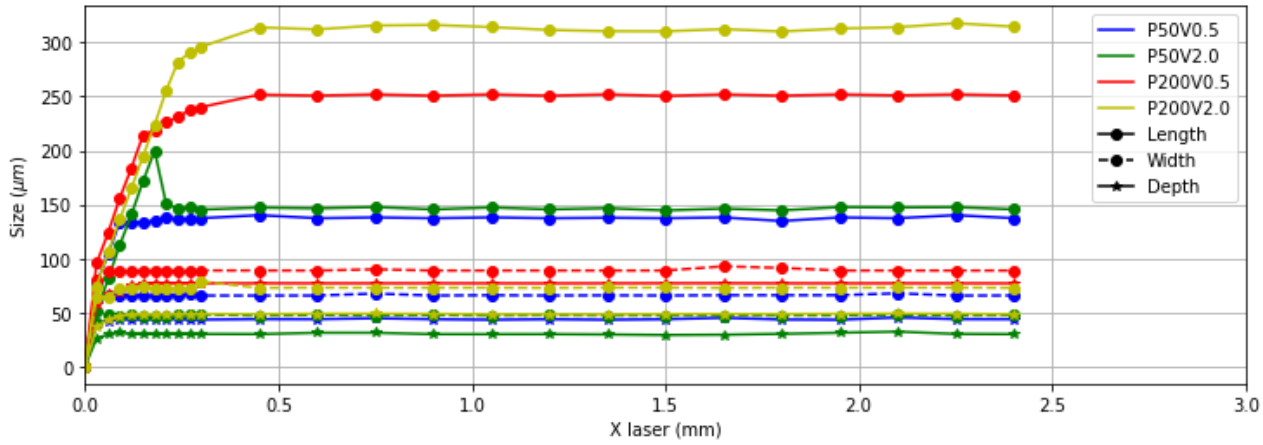

Figure 6. Melt Pool Dimensional Evolution

Then, considering only the average measurements of each melt pool dimension during the stable phase of the process, the results depicted in Figure 7 could be extracted.

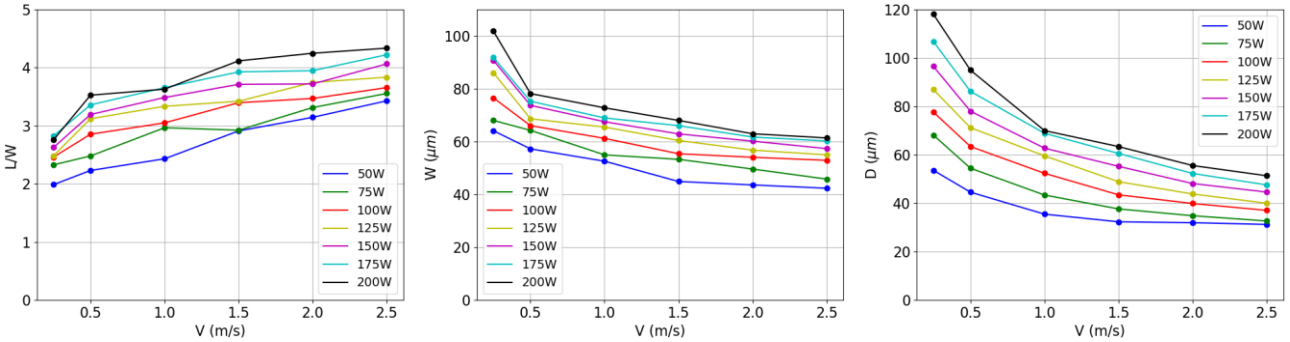

Figure 7. Stable Melt Pool dimensions for different process configurations: Length-width ratio (left); Width (center); Depth (right)

By comparing the calculated dimensions to the defined quality thresholds, the viability of each laser parameter combination could be estimated. Then, using the assigned scores, it was possible to generate the process maps presented in Figure 8 by interpolating linearly between the simulated points which are represented by the white dots. The map for

30µm powder layers shows good similarity to the graph presented in Figure 3, demonstrating the validity of the calibrated numerical model for generating estimates about the printing process. Moreover, the map for 50µm, generated with results from a second model with an increased layer thickness, demonstrates the usefulness of the simulations in exploring new process configurations by quickly indicating promising parameter combinations.

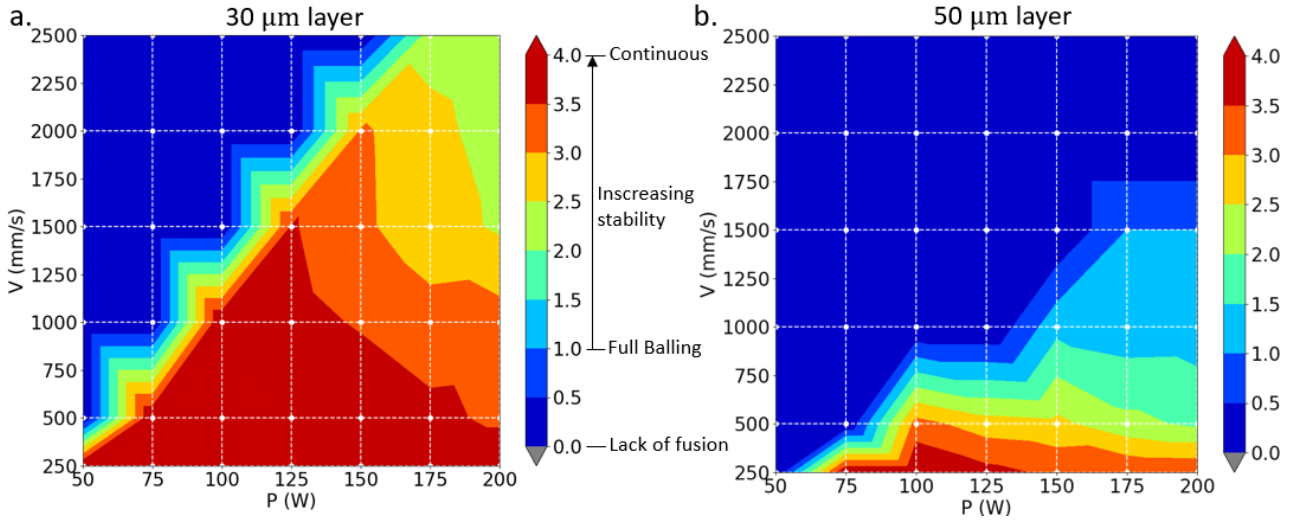

Figure 8. Process Map based on numerical results: (a) 30µm powder layer; (b) 50µm powder layer

4. CONCLUSIONS

The development of a simple yet powerful numerical model for the Remanium Star alloy has been achieved. This model provides a valuable tool for simulating and increasing understanding of the additive manufacturing process using this specific alloy. It is capable of providing good insights into the process, its underlying mechanisms and the impact of different parameter combinations, facilitating the selection of suitable printing parameters to achieve the desired outcomes. Process maps may be estimated for new untested configurations, such as higher layer thicknesses, allowing a much quicker development of new printing procedures.

Moreover, the calibration of the model was successfully performed using just simple experiments. This demonstrates that even with limited experimental data, it is possible to achieve valuable results and predictions.

In conclusion, the developed numerical model for the Remanium Star alloy already presents a valuable tool for the additive manufacturing community. Its simplicity and effectiveness, combined with the ability to be calibrated with limited experimental data, makes it a practical and reliable solution. The insights provided by the model contribute to process optimization and parameter selection, ultimately improving the quality and efficiency of the printing process.

In the future, the present research may be extended by further studying and modelling the other levels of the process: full layer formation with the interaction between tracks and the full volumetric build. Moreover, the impact of other parameters other than laser power and speed may be focused in more depth as well as other phenomena such as the keyhole mode induced defects.

5. ACKNOWLEDGEMENTS

Partial funding by Petrogal-Brasil through ANP and EMBRAPII, PDI project no. GALP 38 with COPPETEC Foundation, and the sponsoring agencies CNPq and FAPERJ are gratefully acknowledged.

6. REFERENCES

Batchelor, G. & O'Brien, Richard. (1977). Thermal or Electrical Conduction Through a Granular Material. Proceedings of The Royal Society A: Mathematical, Physical and Engineering Sciences. 355. 313-333.

Bidare, P., Bitharas, I., Ward, R.M., Attallah, M.M., Moore, A.J., Fluid and particle dynamics in laser powder bed fusion, Acta Materialia, Volume 142, 2018, Pages 107-120, ISSN 1359-6454

De Moraes, D.A.; Czekanski, A. Parametric Thermal FE Analysis on the Laser Power Input and Powder Effective Thermal Conductivity during Selective Laser Melting of SS304L. J. Manuf. Mater. Process. 2018, 2, 47

Dentarum, Remanium star powder instructions, 2022, https://www.dentaurum.de/files/989-802-58.pdf

Gunenthiram, Valérie & Peyre, Patrice & Schneider, Matthieu & Dal, Morgan & Frederic, Coste & Fabbro, Remy. (2017). Analysis of laser–melt pool–powder bed interaction during the selective laser melting of a stainless steel. Journal of Laser Applications. 29.

Gusarov, A. & Yadroitsev, Igor & Bertrand, Ph & Smurov, I.. (2009). Model of Radiation and Heat Transfer in Laser-Powder Interaction Zone at Selective Laser Melting. Journal of Heat Transfer.

Interreg Sudoe programme, (2019). Effect of printing conditions on porosity formation in powder bed melting of Ti-6Al-4V parts : an approach based on 3d x-ray tomography [White Paper]. https://www.samtsudoe.com/wp-content/uploads/2019/09/White-paper1-EN.pdf

Johnson, L., Mahmoudi, M., Zhang, B., Seede, R., Huang, X., Maier, J.T., Maier, H.J., Karaman, I., Elwany, A., Arróyave, R., Assessing printability maps in additive manufacturing of metal alloys, Acta Materialia, Volume 176, 2019, Pages 199-210, ISSN 1359-6454

King, Wayne & Anderson, A. & Ferencz, Robert & Hodge, N. & Kamath, C. & Khairallah, Saad. (2015). Overview of modelling and simulation of metal powder bed fusion process at Lawrence Livermore National Laboratory. Materials Science and Technology.

Loh, L_E., Chua, C-K., Yeong, W-Y., Song, J., Mapar, M., Sing, S-L., Liu, Z-H., Zhang, D-Q., Numerical investigation and an effective modelling on the Selective Laser Melting (SLM) process with aluminium alloy 6061, International Journal of Heat and Mass Transfer, Volume 80, 2015, Pages 288-300, ISSN 0017-9310

Megahed, M., Mindt, HW., N'Dri, N. et al. Metal additive-manufacturing process and residual stress modeling. Integr Mater Manuf Innov 5, 61–93 (2016)

Safdar, S., Pinkerton, A.J., Li, L., Sheikh, M.A., Withers, P.J., An anisotropic enhanced thermal conductivity approach for modelling laser melt pools for Ni-base super alloys, Applied Mathematical Modelling, Volume 37, Issue 3, 2013, Pages 1187-1195, ISSN 0307-904X

Saunders M., Director of Group Strategic Development at Renishaw, Linkedin, 2017, Gone with the wind - how gas flow governs LPBF performance, https://www.linkedin.com/pulse/gone-wind-how-gas-flow-governs-lpbf-performance-marc-saunders, Accessed 26 Oct 2022.

Shahabad, S.I., Zhang, Z., Keshavarzkermani, A. et al. Heat source model calibration for thermal analysis of laser powder-bed fusion. Int J Adv Manuf Technol 106, 3367–3379 (2020)

Siao, Y-H., Wen, C-D., Examination of molten pool with Marangoni flow and evaporation effect by simulation and experiment in selective laser melting, International Communications in Heat and Mass Transfer, Volume 125, 2021, 105325, ISSN 0735-1933

Tolochko, N.K., Khlopkov, Y.V., Mozzharov, S.E., Ignatiev, M.B., Laoui, T. and Titov, V.I. (2000), "Absorptance of powder materials suitable for laser sintering", Rapid Prototyping Journal, Vol. 6 No. 3, pp. 155-161

Wang, X., Laoui, T., Bonse, J. et al. Direct Selective Laser Sintering of Hard Metal Powders: Experimental Study and Simulation. Int J Adv Manuf Technol 19, 351–357 (2002)

Yadroitsev, I., (2009). Selective laser melting: Direct manufacturing of 3D-objects by selective laser melting of metal powders.

Zhang, Z., Huang, Y., Kasinathan, A.R., Shahabad, S.I., Ali, U., Mahmoodkhani, Y., Toyserkani, E., 3-Dimensional heat transfer modeling for laser powder-bed fusion additive manufacturing with volumetric heat sources based on varied thermal conductivity and absorptivity, Optics & Laser Technology, Volume 109, 2019, Pages 297-312, ISSN 0030-3992, ISSN 0030-3992

7. RESPONSIBILITY NOTICE

The authors are the only responsible for the printed material included in this paper.